Journal Name

Dynamic Article Links ▶

Cite this: DOI: 10.1039/c0xx00000x

www.rsc.org/xxxxxx

ARTICLE TYPE

Intermolecular Interaction Influence on Solid State Luminescence of Imidazopyrizines : Theoretical Interpretations using FMO-TDDFT and ONIOM Approach

Yasuhiro Shigemitsu,*[a,b] Toshiki Mutai[c] , Hirohiko Houjou[d] and Koji Araki[e]

Received (in XXX, XXX) Xth XXXXXXXXX 20XX, Accepted Xth XXXXXXXXX 20XX
DOI: 10.1039/b000000x

6-cyano-2-(2′-hydroxyphenyl)imidazo[1,2-a]-pyridine (6CN-HPIP) shows polymorph-dependent luminescence with the three different crystal forms exhibiting the packing-controlled bright colors turning, orange, yellow, and red. The distinctive emission in aggregated states was treated with finite cluster models and analyzed by means of quantum chemistry calculations. Influence of structural displacements and intermolecular interactions in crystalline state were examined in detail on the solid state luminescence by using Fragment Molecular Orbital (FMO) scheme, suitable for studies of aggregated molecular systems. The FMO pair interaction analysis of the S_1-S_0 emission maxima indicated that the intermolecular side-to-side interactions provoke hypsochromic shifts; facial interactions induce bathochromic shifts; crystal packing effects in total induce hypsochromic shifts. The FMO predictions of the emission maxima offered qualitatively satisfactory agreements with the experiments. However, the small cluster models including up to the 17 molecules did not reach quantitative convergence, i.e., the emission colour order among them were not well reproduced.

1. Introduction

Electronic excited state properties of functional dyes have been widely studied and their fluorescence has attracted a broad range of interests in industrial applications such as new textiles, emissive molecular probes in diagnoses, light-emitting diodes (OLED).[1-4] Especially, applications based on the tuning and switching of solid-state luminescence draws considerable attentions and packing-turned luminescence molecules have been increasingly reported. In general, fluorescent compounds show intense luminescence in dilute solution while fairly weak or nonluminescent in the crystalline state, due to enhanced nonemissive deactivation channels such as exciton/excimer formation, vibronic interactions and other nonradiative decay processes in aggregated states. Interestingly, many opposite phenomena have been reported today to the conventional emission quenching, where strong luminescence is observed in the solid state whereas negligible luminescence in dilute solution. This anomaly is called Aggregation Induced Emission Enhancement (AIEE).[5-7]

Computational molecular design of fluorescent dyes is directed to realize a number of requirements; large quantum yields, small overlap between absorption and emission spectra, photochemical stability and others. Modern ab initio quantum chemistry methods allow for determining a large set of properties in chemical accuracies for molecular systems in their ground state. Predictions of excited-state properties such as fluorescence and phosphorescence are, however, still challenging tasks. Reliable post-Hatree-Fock approaches such as SAC-CI,[8] EOM-CC,[9] CAS-PT2,[10] are too expensive to be directly applied to realistic large chemical systems in excited states owing to the inherent high accuracy/cost ratio. Time-dependent density functional theory (TD-DFT), the linear response approach applied to DFT, is rapidly emerging as a promising alternative for the evaluation of excited-state geometries and properties. Modern TD-DFT methods have been confirmed to achieve excellent performance that is compatible with more computationally demanding wavefunction-based methods. [11] For condensed phase systems, a sophisticated treatment of a large complex system is required to understand AIEE but such state-of-the-art methodologies are still in an immature stage. In order to circumvent huge computational costs for direct treatment of whole large systems, modern quantum chemistry techniques are based on the idea to divide them into fragments [12-13] or to hybridize several theoretical levels allocated to multiply divided layers such as QM/MM[14] or ONIOM.[15] A series of computational studies were reported using QM/MM approach[16-18] in the prediction of luminescence in solid

states related to AIEE.

We previously reported polymorph-dependent luminescence of 2-(2′-hydroxyphenyl)imidazo[1,2-a]-pyridine (HPIP) which shows very weak fluorescence with a large Stoke's shift in apolar solvent which is ascribed to excited-state intramolecular proton transfer (ES-IPT) emission.[19] The two crystal HPIP polymorphs exhibit bright luminescence of two different colors, blue-green and yellow. DFT and MS-CASPT2 calculations for an isolated HPIP have been attempted to elucidate the origin of emission enhancement as well as possible mechanism for the packing-controlled luminescence color tuning, where the potential energy surfaces in the S_0 and S_1 states were explored by means of CASSCF level of theory to find Conical Intersections (CIs) which plays an important role in the luminescent properties of HPIP.[20] Still, the aggregation effects on the solid-state luminescence of HPIP crystals are not satisfactory elucidated because of MS-CASPT2 limitations in a direct application to huge aggregates.

In the present computational study, we aim to elucidate the polymorph-dependent luminescence of 6CN-HPIP[21], bearing a cyano group at a 6-position of HPIP. The molecule shows three colored luminescence (yellow, orange, red) in the solid state specific to the corresponding the respective polymorphs, as shown in Figure 1. The X-ray crystallographic analysis indicated the difference in the molecular packing should be a dominant factor of the polymorph dependence of the ESIPT luminescence [22], as shown in Figure 2. The emission maxima of the compound in the three different polymorphs were computationally evaluated by means of ONIOM and FMO-TDDFT[23] approach applied to the finite cluster models. The cluster size dependent evolutions were analyzed on the neighboring fragment-fragment interactions in details based on fragment analysis.

2. Computational Details

The geometry optimizations in S_1 were carried out using TDDFT(B3LYP)/6-31+G(d) and 4 state-averaged(SA)-CASSCF(8e,8o)/ANO-L, respectively in vacuo. The $S_1 \rightarrow S_0$ vertical transition energies of an isolated 6CN-HPIP in keto form with the geometry being fixed in planar form, which is supposed to be the responsible emissive S_1 state. The CASSCF calculations include near-frontier π orbitals (HOMO-3 to HOMO and LUMO to LUMO+3). The structures corresponding to the local minima were confirmed by harmonic frequency analysis. The single point CASSCF(10,10)/ANO-L and MS-CASPT2(10e,10o)/ANO-L level of theory were also employed to evaluate the $S_1 \rightarrow S_0$ vertical transition energies where the extended active spaces include HOMO-5 n-orbitals and the two π virtual orbitals to include the n-π* mixing in a balanced way. The excitation character was verified to possess overwhelming HOMO → LUMO excitation coefficients. The 4 SA-CASSCF(10e,10o) calculations were done and the 4 single-state (SS)-CASPT2(10e,10o) states were further averaged within MS-CASPT2 scheme. The level shift technique with careful choice of shift value (0.3) seems to work well with the fairly large reference weight of the main configuration. The $S_1 \rightarrow S_0$ vertical transition energies were evaluated at TDDFT/6-31+G(d) level using two XC(exchange correlation)-functionals, i.e., B3LYP and CAM-B3LYP.[24] CAM-B3LYP has been reported to be suitable to predict the excited state conical intersection geometries,[25] electronic absorption/emission energies,[26-27] especially for delocalized excited states. [28-29]

The cluster models of 2-O, 2-Y and 2-R as shown in Figure 3 were extracted from the crystallographic data, containing 17 molecules, within around 8 Å apart from the center of mass of the central keto molecule. The cluster models in the S_1 state were created through manipulation of the S_0 cluster models, in which the geometries were partially optimized by TDDFT(B3LYP)/6-31+G(d) only for the central keto molecule with the surrounding molecules fixed in the S_0 geometry treated by semiempirical PM3 level, i.e., two-layer ONIOM (TD(B3LYP)/6-31+G(d): PM3). The $S_1 \rightarrow S_0$ vertical transition energies were evaluated by means of ONIOM single point calculations for the optimized geometries (TDDFT(CAM-B3LYP)/6-31G(d):PM3). This modeling has been already studied as *a frozen-molecule approximation*.[30] The partial geometry optimization with the surrounding PM3 regions fixed has been rationalized by Shuai et al. using QM/MM cluster models for 3-cyano-2-phenyl-Z-NH-indole crysltals.[18] FMO-TDDFT single point calculations were done in order to estimate the $S_1 \rightarrow S_0$ energies, using CAM-B3LYP functional for the ONIOM-optimized geometries abovemensioned. The FMO-TDDFT calculations employed 6-31G(d) throughout the present study since the more extended basis sets larger than 6-31+G(d) suffered from FMO convergence failure. The emission maxima and intermolecular interactions were evaluated at the two FMO levels; FMO-1 (including only monomer interactions)[23] and FMO-2 (including up to dimer interactions).[31] In the present study, the emission energies were commonly estimated by vertical $S_1 \rightarrow S_0$ transitions (electronic energy differences between ground and excited states at ground state optimized geometries). The gaps among vertical, adiabatic (the differences between the states at respective optimized geometries), 0-0 (the differences between the states in the lowest vibrational energy levels) transition energies are expected to be uniformly method-insensitive, as illustrated by the energies of green fluorescence protein[32]. A correction to basis set superposition errors (BSSE) were not considered in the present calculations. CASSCF and MS-CASPT2 calculations were performed using MOLCAS 7.4 software.[33-34] DFT, TD-DFT and ONIOM calculations using Gaussian 09 software,[35] FMO-TDDFT calculations using GAMESS ver.2012, [36] respectively.

3. Results and Discussion

3.1 Isolated 6CN-HPIP: method validation

A series of computations by means of TDDFT, CASSCF and MS-CASPT2 for 6CN-HPIP in vacuo are shown in Table 1, in aiming to validate the prediction accuracies of the computed $S_1 \rightarrow S_0$ vertical transition energies. The gap between MS-CASPT2//CASSCF and MS-CASPT2//TDDFT was 31 nm, which means that a qualitatively correct geometry was obtained at TDDFT(B3LYP)/6-31+G(d) level geometry optimization. It is reported that B3LYP functional substantially underestimates the $S_1 \rightarrow S_0$ gap while CAM-B3LYP gives a quantitative agreement with that of MS-CASPT2, as reported previously. [28-29]

3.2 ONOM results

The ONIOM calculations for 2-O, 2-Y, 2-R were performed respectively, i.e., for monomer (one keto 6CN-HPIPs in the S_1 (TDDFT): 16 enol 6CN-HPIPs in the S_0 (PM3)) and dimer (a pair of a keto and an enol (TDDFT): 15 enols (PM3)), as shown in Table 2. The aggregation effects on the spectra were taken into account through TDDFT and PM3 interlayer interactions within the ONIOM model. Intermolecular charge transfer excitation and extonic effects across TDDFT-PM3 regions were ignored as well as crystal field effect from infinite electrostatic interactions.

The predicted λ_{max} of 2-Y, 2-R, 2-O did not coincidence with the experiment 2-Y, 2-O, 2-R in low energy order with the monomer ONIOM model. The order was correctly altered for the dimer ONIOM model. In comparison with the results of the bare monomer and the monomer ONIOM model, the surrounding 16 enols treated by PM3 exert slightly on the emission peak shift within 2 nm. This indicates that the dimer interactions between the keto form and the enol forms, not the perturbations from the surrounding molecules, play dominant roles in the emission colour in the crystalline state. The gap of theoretical emission maxima between monomer and dimer were not systematic, that is, 2-Y and 2-O showed substantial blue shifts while 2-R showed red shifts. As shown in Figure 2, 2-Y and 2-R are stacked in parallel while 2-O stacked in antiparallel. Upon the excitation, the keto form undergoes strong intramolecular charge transfer associated with the inversion of dipole moment and then the keto embedded in parallel stacked 2-Y crystal and 2-R crystal in S_1 state are stabilized while the keto in antiparallel stacked 2-O crystal is destabilized. In turn, the emission maxima of 2-Y and 2-R are expected to show bathochromic shifts while that of 2-O to shift hypsochromically. However, the hypsochromic shift of 2-Y in experiment was not consistent with this heuristic consideration and the reason for that remain unclear. The intermolecular interactions of the π-stacked IPT pair and the surrounding enol molecules might be a decisive factor of the emission energy in the crystalline polymorphs as well. The remarkably different direction of the dipole moments of the ESIPT and IPT states might be the reason for the sensitive polymorph dependence of the luminescence color, as the energy level of the two states would shift differently upon variation of the environment, and result in the sensitive changing the energy gap. The surrounding PM3 shells gave non-negligibly bathochromic shift on the peak positions through the geometry optimizations. This implies that the structural deformations of the emissive S_1 keto immersed in PM3 shells work effectively on the spectral shift, in comparison with the computed λ_{max} of the monomer 2-Y, 2-O, 2-R and those of the planar keto form. The ONIOM-optimized key geometries among the keto form of 2-Y, 2-O, 2-R are illustrated in Figure 4, which shows that the longer bond length O1-H9 cause the more bathochromic shift of the $S_1 \rightarrow S_0$ peak. This is owing to the tightly constrained keto structure which destabilizes the molecule, leading to narrow the HOMO-LUMO gap.

3.3 FMO-TDDFT results

It is desirable to treat the whole cluster model in chemical accuracy beyond ONIOM scheme for further accurate predictions. Since straightforward TDDFT treatment for the whole system is unfeasible, FMO-TDDFT method was employed to treat the whole system quantum mechanically aiming to circumvent huge computational burden.

The FMO-TDDFT excitations energy ω can be expanded in a similar manner to the FMO energy in the ground state, assuming that the excitation is well localized within a fragment M:

$$\omega = \omega_M + \sum_{I \neq M} (\omega_{MI} - \omega_M) + \ldots \qquad (1)$$

,where the dimer contributions $\omega_{MI} = E^*_{MI} - E^0_{MI}$ correct the monomer excitation energy $\omega_M = E^*_M - E^0_M$. The truncations of the hierarchical expansion up to the first term (FMO1-TDDFT) or up to the second term (FMO2-TDDFT) give the approximate expression as follows, respectively.

$$\omega = \omega_M \qquad (\mathrm{FMO}-1)$$

$$\omega = \omega_M + \sum_{I \neq M} (\omega_{MI} - \omega_M) \qquad (\mathrm{FMO}-2)$$

At FMO1 level, the excitation is localized within the fragment M under the electrostatic field exerted from the surrounding fragments I with the ground state electronic densities remained. At FMO2 level, the dimer pairs are computed and the correction terms $\delta\omega_{MI} = \omega_{MI} - \omega_M$ are summed up to ω_M.

From a computational efficiency viewpoint, FMO-TDDFT timing scale approximately linearly[13] in contrast with conventional full-TDDFT which suffers from the inherent $O(N^3)$ scaling. This FMO-TDDFT efficiency is fully utilized in the present study to carry out the whole quantum chemical treatments of the cluster models.

Single point FMO-TDDFT computations were done for the ONIOM-optimized geometries abovemensioned. The cluster size dependencies of the $S_1 \rightarrow S_0$ emission wavelengths from monomer (one keto form) up to 17 molecules (the one keto surrounded by the 16 enols) were investigated, as shown in Table 3. Comparing the monomer and the dimer results, the gap of theoretical λ_{max} were not systematic for the three models, as the same tendency as ONIOM results. That is, 2-Y and 2-O showed substantial blue shifts while 2-R did a red shift. On the λ_{max} evolutions with the cluster size, the emission peak of 2-R monomer shifted by nearly 30 nm bathochromically toward the pentamers of which the keto is stacked among the 4 enols. The pentamers of 2-Y and 2-O showed the hypsochromic shifts conversely. The emission peaks for the larger cluster sizes exhibited hypsochromic shifts by over 100 nm for the largest 17 molecules consistently for the three models. The large hypsochromic jump was predicted at 13 clusters for 2-R where the central layer containing the keto was horizontally sandwiched by the neighbouring two layers, as shown in Figure 5. The drastic hypsochromic shifts were observed as well for 2-Y and 2-O between the 5 and the 9 and the 9 and 13 clusters, respectively. These jumps appeared using both FMO-1 and FMO-2 therefore the gaps were derived from the pure S_1-S_0 gap narrowing of the S_1 keto immersed in electrostatic field created by the surrounding fragments (FMO-1), not the interfragment dimer interactions (FMO-2). The λ_{max} gap between the FMO-1 predictions with those of FMO-2 seemed to converge toward hypsochromic effect. For small clusters less than 9 clusters the gaps were non-systematic, but the gap between 13

and 17 clusters showed blue shifts commonly for the three crystals by including the dimer interactions. The individual interfragment interactions exerted on the emissive keto are shown in Table 4. The dominant blue shifts were invoked by the pair interactions with Frag-11 (2-O), Frag-9 (2-Y), Frag-10 (2-R), as illustrated in Figure 6, 7, 8, respectively. The hypsochromic contributions come from side-to-side or twisted aligned pairs. The π–π stacking interactions, conversely, serves as red shift contributors; for example, Frag-7 (2-O), Frag-6 (2-Y), Frag-17 (2-R). It looks strange that the face-to-face pair interactions invoked bathochromic shifts consistently while the interactions invoked the hypsochromic (bathochromic) shift for 2-O, 2-Y, (2-R) for the bare dimers abovemensioned. Specifically for 2-O and 2-Y, the face-to-face staking interactions might work in a different way between a pure dimer model and an embedded one where the dimer interactions are influenced by the electrostatic field exerted from the surrounding fragments.

4. Conclusions

The cluster models of the three polymorph-dependent emissive crystals were computationally analyzed by ONIOM and FMO-TDDFT. The crystals exhibited its emission maxima at 548 (yellow), 570 (orange), 585 nm (red), respectively in experiment.[21] The polymorph-dependent luminescence are supposedly influenced by the three competing effects; structural deformation, crystal field, specific intermolecular interactions. The pioneering FMO-TDDFT calculations by Fukunaga et al. for the electronic absorption energies of quinacridone in solid states indicated that three effects are almost equally influential on the spectra peak positions.[37] In the present study, the ONIOM influence on the emission maxima derived from the surrounding molecules is quite marginal within several nm shifts. This minor influence indicates that the substantial ONIOM influence comes from the geometrical deviations in the S_1 state by the surrounding molecules, not from the direct perturbation to the electronic state of the emissive molecule. The FMO-TDDFT analysis showed the significant roles of intermolecular dimer interactions in the emission spectra, which strongly depend on the molecular orientations and mode of packing. Intermolecular hydrogen bonds invoked red shifts whereas stacking interactions induced blue shift. The overall packing effects treated by FMO2-TDDFT invoked blue shift, commonly for the three polymorphs.

The remarkable polymorph dependence of the luminescence color demonstrates that the ESIPT process is a promising mechanism for packing-directed luminescence control, offering a novel design concept for tunable organic luminescent solids. The present study has pioneered the promising role of computational design of AIEE systems by means of FMO-TDDFT.

References

1 K.Shirai, M.Matsuoka, K.Fukunishi, *Dye Pigment*, 2000, **47**, 107-115.

2 K-C.Tang, M-J. Chang, T-Y. Lin, H-A. Pan, T-C.Fang, K-Y. Chen, et al. *J Am Chem Soc*,. 2011, **133**, 17738-17745.

3 Q.Zhang, J.Li, K.Shizu, S.Huang, S.Hirata, H.Miyazaki, et al. *J Am Chem Soc*,. 2012, **134**, 14706-14709.

4 L.Wang, B.Xu, J.Zhang, Y.Dong, S.Wen, H.Zhang, W.Tian, *Phys.Chem.Chem.Phys.*, 2013, **15**, 2449-2458.

5 B-K. An, S-K . Kwon, S-D. Jung, S-Y. Park, *J Am Chem Soc*,. 2002, **124**, 14410-14415.

6 X. Feng, B. Tong, J. Shen, J. Shi, T. Han, L. Chen, et al. *J Phys Chem B*, 2010, **114**, 16731-16736.

7 S.Kamino, A.Muranaka, M.Murakami, A.Tatsumi, N.Nagaoka, Y.Shirasaki, K.Watanabe, K.Yoshida, J.Horigome, S.Komeda, M.Uchiyama, S.Enomoto, *Phys.Chem.Chem.Phys.*, 2013, **15**, 2131-2140.

8 H. Nakatsuji, in Computational Chemistry: Reviews of Current Trends, Ed. J. Leszczynski, Vol. 2 (World Scientific, Singapore, 1997) 62-124.

9. J. F. Stanton and R. J. Bartlett, J. Chem. Phys., 1993, **98**, 7029-39.

10 P.Pulay, *Int.J.Quant.Chem.*, 2011, *111*, 3273–3279.

11 L.Gonzalèz, D.Escudero, L.Serrano-Andrès, *Chem.Phys.Chem.*, 2012, **13**, 28-51; D. Jacquemin, V. Wathelet, E.A.Perpète, C.Adamo, *J. Chem. Theory Comput*,. 2009, **5**, 2420–2435.; D. Jacquemin, V. Wathelet, E.A.Perpète, C.Adamo. *Int. J. Quant. Chem.* 2010, **110**, 2121–2129.

12 K. Kitaura, E. Ikeo, T. Asada, T. Nakano, M. Uebayasi, *Chem Phys Lett.*, 1999, **313**, 701-706.

13. K. Kitaura, D.G. Fedrov, editors. *The fragment molecular orbital method*. New York: CRC Press; 2009. And references theirin

14 S. Canuto, J.R.Sabin, editors. *Combining quantum mechanics and molecular mechanics. Some recent progresses in QM/MM methods. Advances in quantum chemistry*, vol. 59. Academic Press, 2011 and references therein.

15 S. Dapprich, I. Komáromi, KS. Byun, K. Morokuma, MJ. Frisch, *J Mol Struct (Theochem)*, 1999, 462, 1-21.

16 J. Wang, J. Gu, J. Leszczynski, *J.Phys.Chem.A*, 2011, **115**, 6376-6382.

17 Q. Wu, Q. Peng, Y. Niu, X. Gao, Z. Shuai, *J.Phys.Chem. A*, 2012, **116**, 3881-3888.

18 Q. Wu, C. Deng, Q. Peng, Y. Niu ; Z. Shuai, *J.Comput.Chem*,. 2012, **33**, 1862-1869.

19 T. Mutai, H. Tomoda, T. Ohkawa, Y. Yabe, K. Araki. *Angew. Chem. Int. Ed.* 2008, **47**, 9522-9524.

20 Y. Shigemitsu, T. Mutai, H. Houjou, K. Araki, *J. Phys. Chem,. A*, 2012, **116**, 12041–12048.

21 T.Mutai, H.Sawatani, T.Shida, H.Shono, K.Araki, *J.Org.Chem.*, 2013, **78**, 2482-2489.

22 T.Mutai, H.Shono, Y.Shigemitsu, K.Araki, *Cryst.Eng.Comm.*, submitted.

23 M.Chiba, D.G.Fedorov, K.Kitaura, *Chem.Phys.Lett.* , 2007, **444**, 346-350.

24 T. Yanai, D. Tew, N. Handy, *Chem. Phys. Lett.*, 2004, **393**, 51-57.

25 M.Filatov, *J.Chem.Theory.Compt.*, 2013, **9**, 4526-4541.

26 D.Jacquemin, A.Planchat, C.Adamo, B.Mennucci, *J.Chem.Theory.Compt.*, 2012, **8**, 2359-2372.

27 C.A.Guido, S.Kecht, J.Kongstad, B.Mennucci, *J.Chem.Theory.Compt.*, 2013, **9**, 2209-2220.

28 D. Jacquemin, E.A. Perpète, G.E. Scuseria, I. Ciofini, C. Adamo, *J. Chem. Theory Comput.* 2008, **4**, 123-135.

29 C.A. Guido, D. Jacquemin, C. Adamo, B. Mennucci, *J.Phys.Chem.A*, 2010,**114**, 13402–13410.

30 M-C. Li, M. Hayashi , S-H. Lin, *J Phys Chem A*, 2011, **115**, 14531-14538.

31 M.Chiba, D.G.Fedorov, K.Kitaura, *J.Chem.Phys.*, 2007, **127**, 104108.

32 M.Uppsten, B.Durbeej, *J.Comp.Chem.*, 2012, **33**, 1892.

33 MOLCAS ver.7.4, Lund University, 2008; F. Aquilante, L.De. Vico, N. Ferré, G. Ghigo, P.-Å. Målmqvist, P. Neogrády, T.B. Pedersen, M. Pitonak, M. Reiher, B.O. Roos, L. Serrano-Andrés, M. Urban, V.Veryazov, R. Lindh, *J.Comp.Chem.*, 2010, **31**, 224.

34 P.-O. Widmark, P.-A. Målqvist, B.O. Roos, *Theor.Chim.Acta*, 1990, **77**, 291.

35 M.J. Frisch, G.W. Trucks, H.B. Schlegel, G.E. Scuseria, M.A. Robb, J.R. Cheeseman, G. Scalmani, V. Barone, B. Mennucci, G.A. Petersson, H. Nakatsuji, M. Caricato, X. Li, H.P. Hratchian, A.F. Izmaylov, J. Bloino, G.Zheng, J.L. Sonnenberg, M. Hada, M. Ehara, K. Toyota, R. Fukuda, J. Hasegawa, M. Ishida, T. Nakajima, Y. Honda, O. Kitao, H. Nakai, T. Vreven, J.A. Montgomery, Jr., J.E. Peralta, F. Ogliaro, Bearpark, J.J. Heyd,; E. Brothers, K.N. Kudin, V.N. Staroverov, R. Kobayashi, J. Normand, K. Raghavachari, A. Rendell, J.C. Burant, S.S. Iyengar, J. Tomasi, M. Cossi, N. Rega, J.M. Millam, M. Klene, J.E. Knox, J.B. Cross, V. Bakken, C. Adamo, J.

Jaramillo, R. Gomperts, R.E. Stratmann, O. Yazyev, A.J. Austin, R. Cammi, C. Pomelli, J.W. Ochterski, R.L. Martin, K. Morokuma, V.G. Zakrzewski, G.A. Voth, P. Salvador, J.V. Ortiz, J. Cioslowski, D.J. Fox, Gaussian 09 revision B.1, Gaussian Inc. Wallingford CT 2009.

36 M.W.Schmidt, K.K.Baldridge, J.A.Boatz, S.T.Elbert, M.S.Gordon, J.H.Jensen, S.Koseki, N.Matsunaga, K.A.Nguyen, S.Su, T.L.Windus, M.Dupuis, J.A.Montgomery *J. Comput. Chem.*, 1993, **14**, 1347-1363.

37 H. Fukunaga, DG. Fedorov, M. Chiba, K. Nii, K.Kitaura, *J.Phys.Chem.A.*, 2008, **112**, 10887-10894.

Notes and references

[a] *Industrial Technology Center of Nagasaki, 2-1303-8 Ikeda Omura, Nagasaki 856-0026, Japan. E-mail: shige@tc.nagasaki.go.jp*

[b] *Graduate School of Engineering, Nagasaki University, 1-14 Bunkyo-machi 852-8521, Japan.*

[c] *Institute of Industrial Science, University of Tokyo, 4-6-1 Komaba, Meguro-ku, Tokyo 153-8505, Japan. E-mail: mutai@iis.u-tokyo.ac.jp*

[d] *Institute of Industrial Science, University of Tokyo, 4-6-1 Komaba, Meguro-ku, Tokyo 153-8505, Japan. E-mail: houjou@iis.u-tokyo.ac.jp*

[e] *Institute of Industrial Science, University of Tokyo, 4-6-1 Komaba, Meguro-ku, Tokyo 153-8505, Japan. E-mail: araki@iis.u-tokyo.ac.jp*

Figure and Table captions

Figure 1.
Polymorph-dependent three color luminescence of 6CN-HPIP. (Reproduced with permission from reference 22 Copyright RSC.)

Figure 2.
Crystal structures of 2-Y, 2-O and 2-R. (a) ORTEP drawing (b) top view (c) side view, respectively. (Reproduced with permission from reference 22 Copyright RSC.)

Figure 3.
Cluster models for 2-Y, 2-O and 2-R containing 17 6CN-HPIPs. Circles indicate the excited keto form in the S_1 state. (ball & stick representation)

Figure 4.
Key geometrical parameters of 2-O, 2-Y, 2-R. Computationally optimized keto form (upper columns) and experimentally determined enol forms (lower columns)

Figure 5.
Cluster size evolution in the case of 2-R. Circles indicate the excited keto form in the S_1 state.

Figure 6.
FMO2-TDDFT pair interaction analysis for 2-O. Frag-1(keto emissive center), Frag-5, Frag-7, Frag-11, are coloured in red, yellowgreen, yellow, pink, respectively.

Figure 7.
FMO2-TDDFT pair interaction analysis for 2-Y. Frag-1(keto emissive center), Frag-2, Frag-6, Frag-9, are coloured in red, yellowgreen, yellow, pink, respectively.

Figure 8.
FMO2-TDDFT pair interaction analysis for 2-R. Frag-1(keto emissive center), Frag-8, Frag-9, Frag-10, are coloured in red, yellowgreen, yellow, pink, respectively.

Table 1.
Computed S_1-S_0 emission wavelengths (nm) of planar keto form of 6CN-HPIP in vacuo. (Reproduced with permission from reference 22 Copyright RSC.)

Table 2.
Computed S_1-S_0 emission wavelengths (nm) of the ONIOM cluster models for 2-O, 2-Y, 2-R. (Reproduced with permission from reference 22 Copyright RSC.)

Table 3.
Evolution of FMO-TDDFT S_1-S_0 emission wavelengths (nm) depending on the ONIOM cluster sizes for 2-O, 2-Y, 2-R.

Table 4.
Individual dimer contributions to S_1->S_0 emission energies (eV) of the 17 clusters for -O, 2-Y, 2-R by means of FMO2-TDDFT

Figure 1

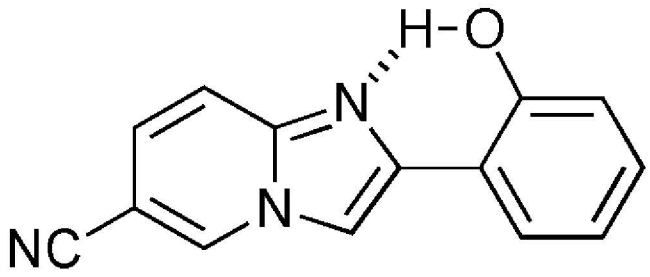

6-Cyano **HPIP** (**2**)

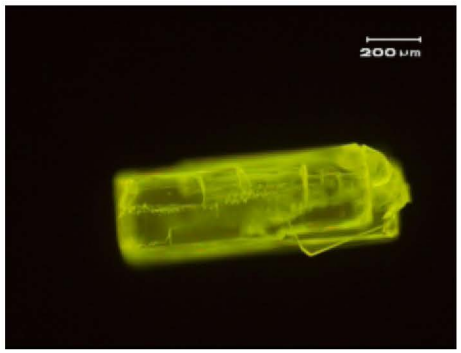

2-Y

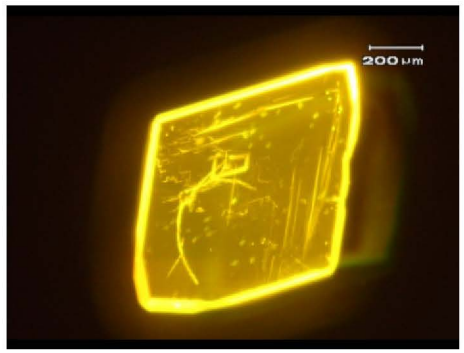

2-O

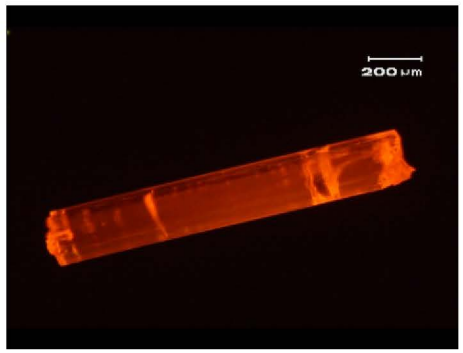

2-R

Figure 2

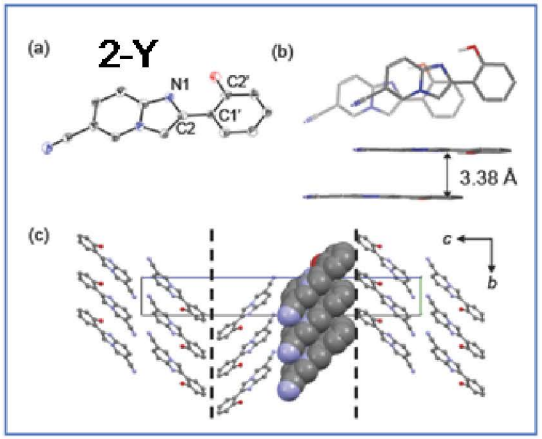

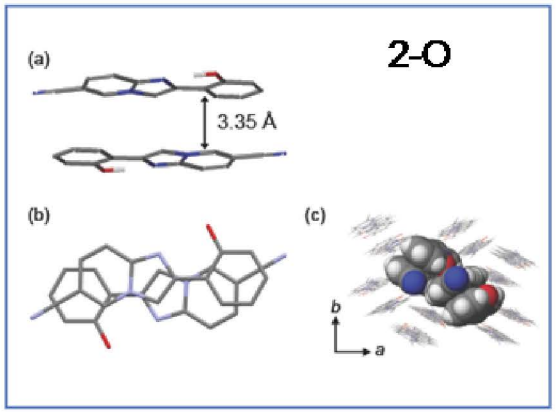

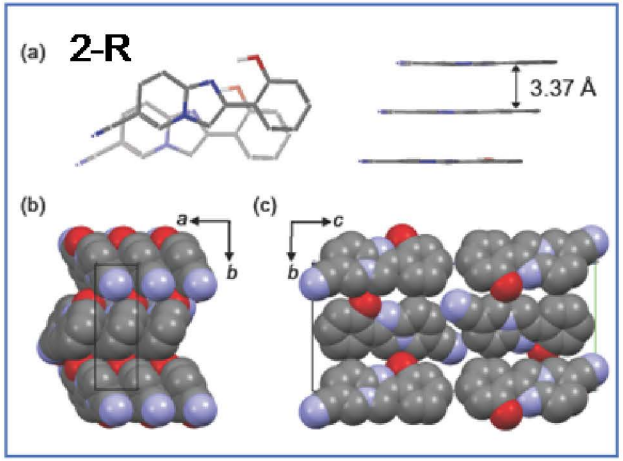

Figure 3

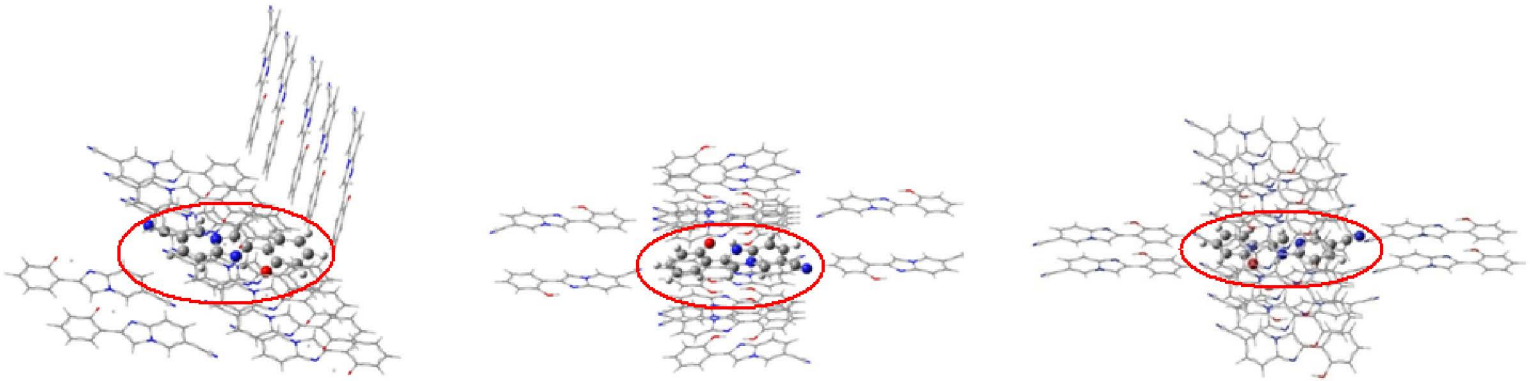

2-Y　　2-O　　2-R

Figure 4

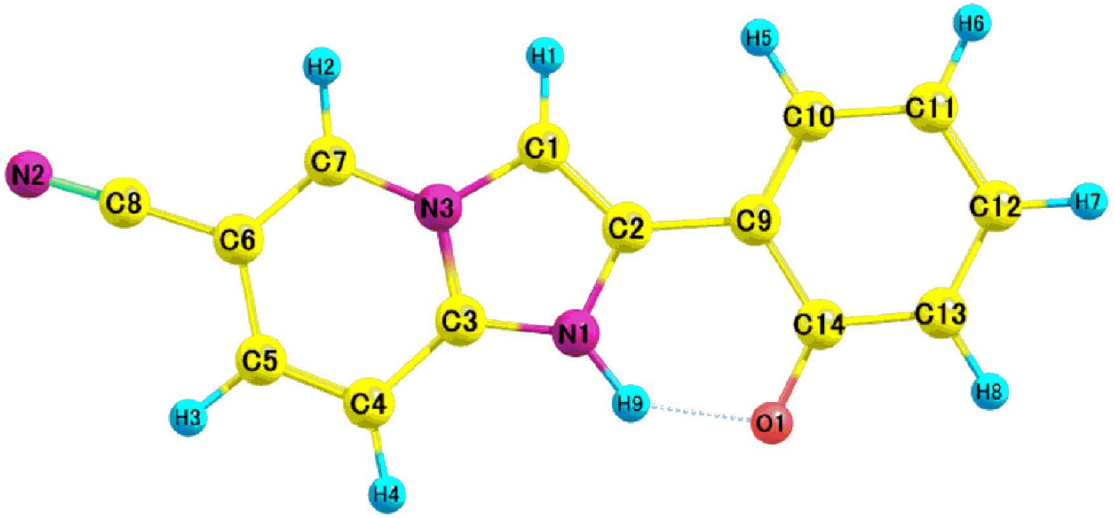

Morph	interatomic distances			twist angle
	r(O1-H9)	r(O1-C14)	r(N1-H9)	ϕ(N1-C2-C9-C14)
2-Y	1.679 1.055	1.291 1.367	1.041 1.588	1.9 1.4
2-O	1.929 0.979	1.280 1.368	1.016 1.728	-3.5 -2.6
2-R	1.820 0.946	1.294 1.365	1.025 1.760	-4.2 -1.4

Figure 5

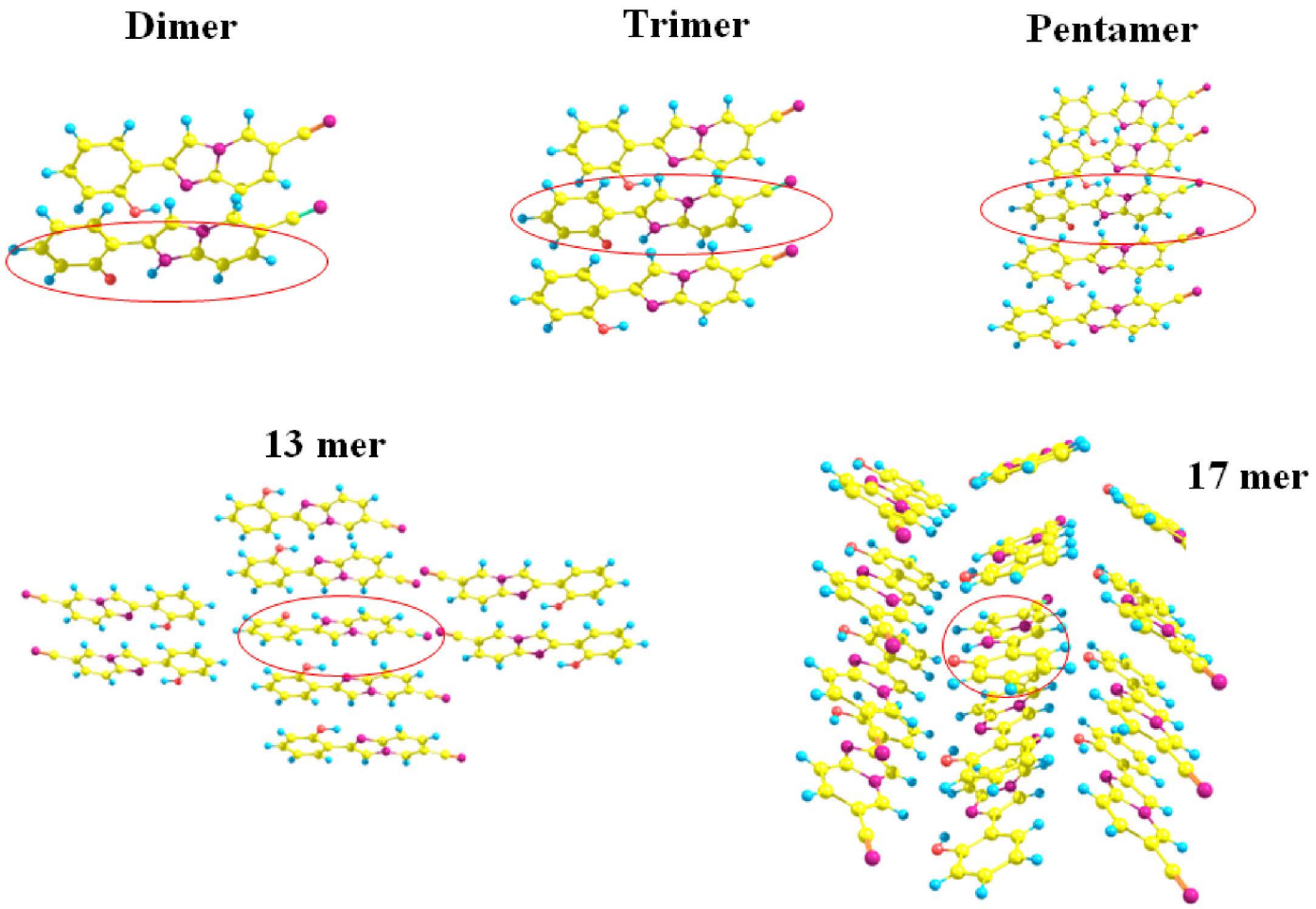

Figure 6

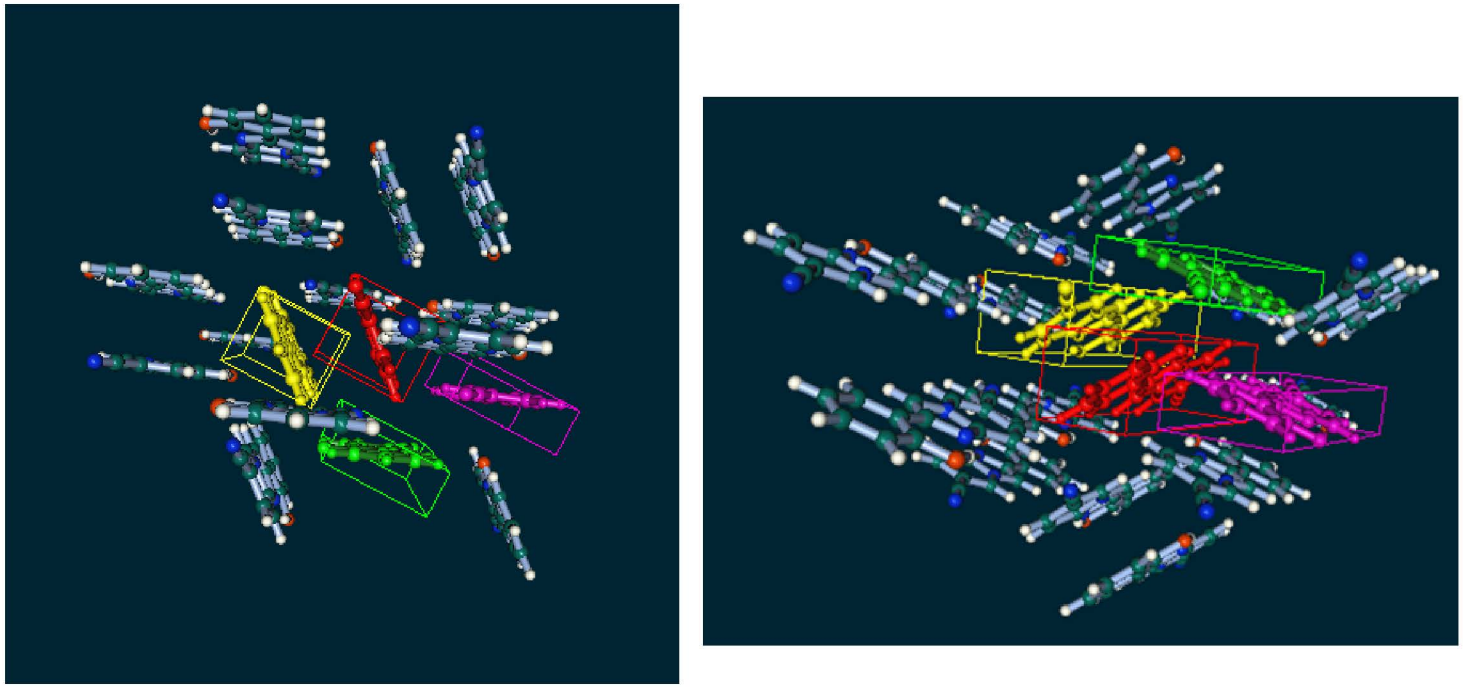

Figure 7

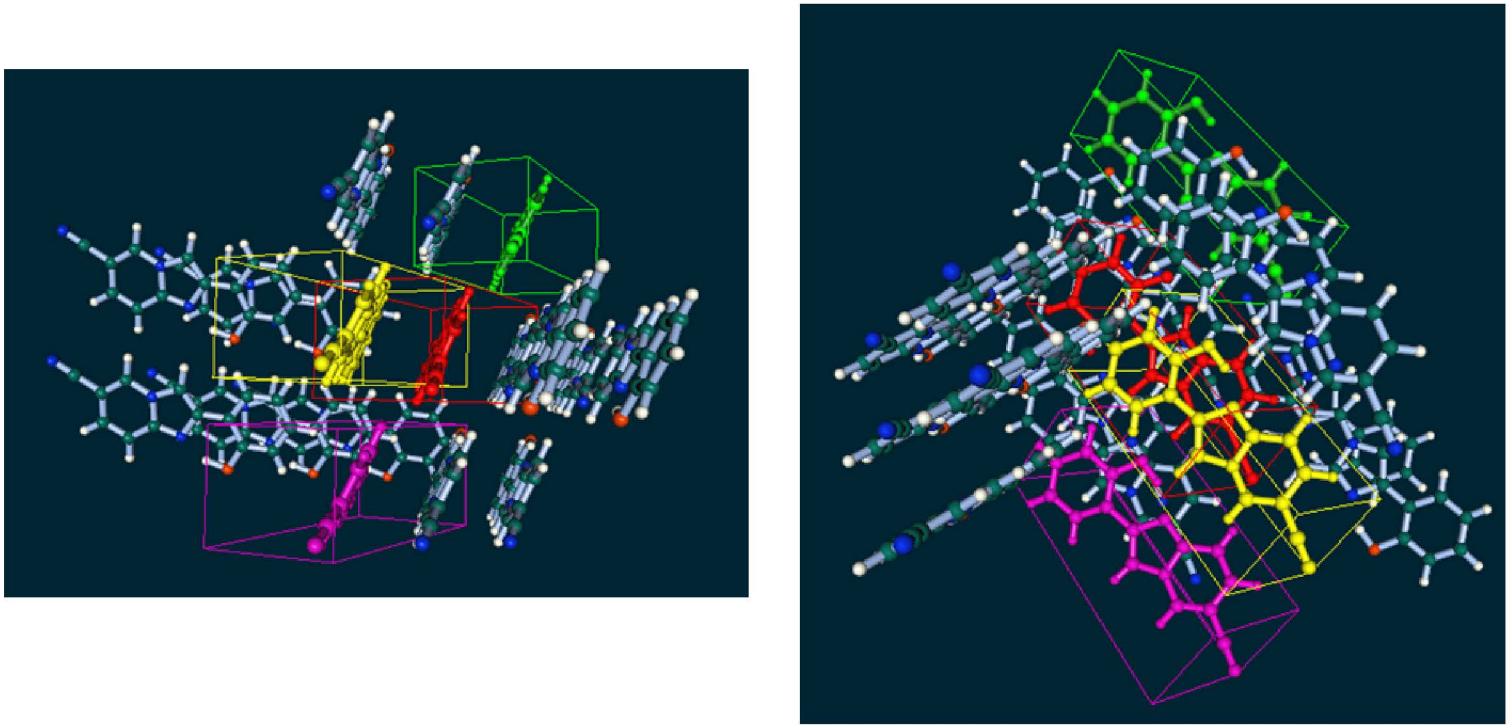

Figure 8

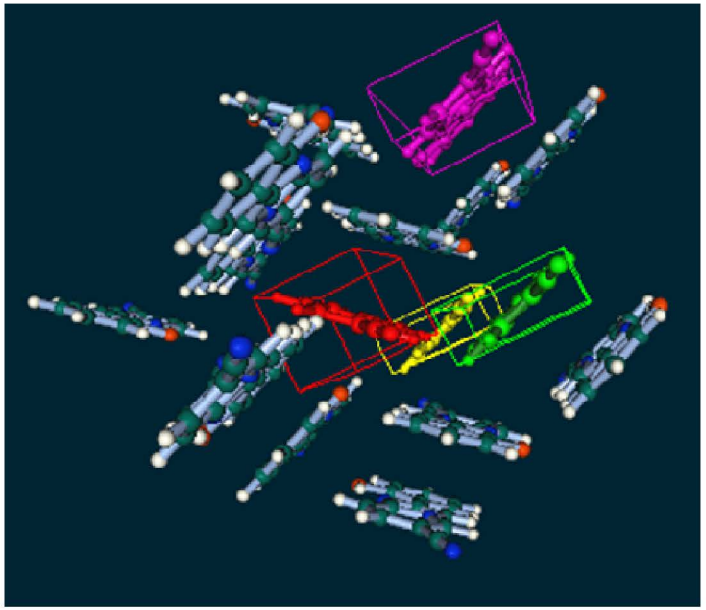

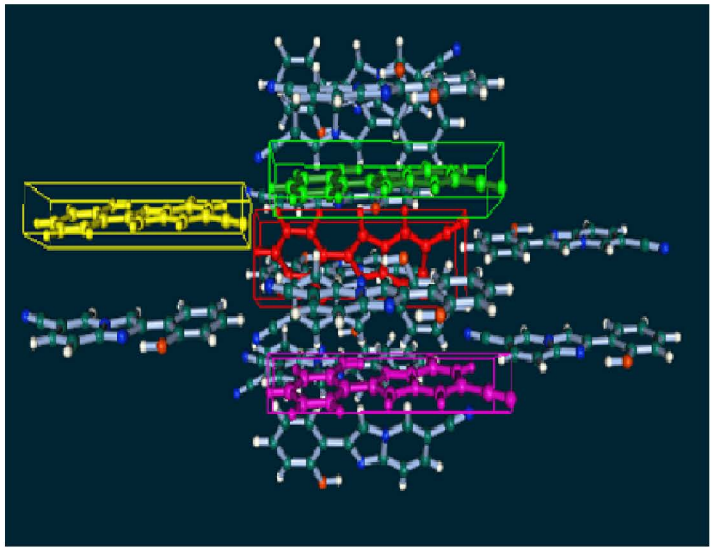

Table 1

Geom-1 [1]				Geom-2 [2]	
TD(B3LYP)[3]	TD(CAM)[4]	CAS[5]	PT2[6]	CAS[5]	PT2[6]
879	544	709	551	1038	582

(1) Optimized geometry at TD(B3LYP)/6-31+G(d)

(2) Optimized geometry at CASSCF(8,8)/ANO-L

(3) TD(B3LYP)/6-31+G(d)

(4) TD(CAM-B3LYP)/6-31+G(d)

(5) 4-SA-CASSCF(10,10)/ANO-L

(6) 4-SA-MS-CASPT2(10,10)/ANO-L

Table 2

	Exp.	Isolated		ONIOM	
		Monomer[1,2]	Dimer[1,2] (keto+enol)	Monomer[2]	Dimer[2]
2-Y	548	542	507	541	506
2-O	570	593	520	591	518
2-R	585	557	588	556	586

(1) Geometries extracted from the optimized cluster models at ONIOM(TD(B3LYP)/6-31+G(d):PM3) level

(2) Higher layer TD(CAM-B3LYP)/6-31G(d) : low layer PM3

Table 3

Morph	Expl.	Monomer[1,2]	Dimer[1,2] (keto+enol pair)	Trimer[1,2] (keto + 2 enol)	5-mer[1,2] (keto + 4 enol)	9mers[1,2] (1-keto+6-enol)	13mers[1,2] (1-keto+12-enol)	17mers[1,2] (1-keto+16-enol)
Y	548	542	507 507	500 502	517 518	453 438	456 444	445 427
O	570	594	520 520	504 504	513 517	500 513	429 427	419 409
R	585	557	580 589	583 597	582 600	576 597	432 423	430 420

(1) Geomerties extracted from the optimized 17 molecules ONIOM model at TD(B3LYP)/6-31+G(d):PM3

(2) FMO1-TDDFT(CAM-B3LYP)/6-31G(d) (in upper column), FMO2-TDDFT(CAM-B3LYP)/6-31G(d) (in lower column)

Table 4

	Contributions (eV)
FRAG1 (keto)	2.962
FRAG5	0.038
FRAG6	0.011
FRAG7	-0.028
FRAG8	0.009
FRAG9	0.009
FRAG11	0.060
FRAG14	-0.009
FRAG15	-0.008
FRAG16	-0.008
Total (FMO2-TDDFT)	3.035

2-O

	Contributions (eV)
FRAG1 (keto)	2.787
FRAG2	0.063
FRAG5	0.010
FRAG6	-0.021
FRAG8	0.005
FRAG9	0.064
FRAG10	0.010
FRAG12	-0.008
FRAG13	-0.008
FRAG16	-0.017
Total (FMO2-TDDFT)	2.904

2-Y

	Contributions (eV)
FRAG1 (keto)	2.881
FRAG3	-0.017
FRAG6	-0.007
FRAG7	0.007
FRAG8	0.036
FRAG9	0.040
FRAG10	0.056
FRAG11	-0.010
FRAG16	0.015
FRAG17	-0.041
Total (FMO2-TDDFT)	2.954

2-R